SCIENCE CHINA
Technological Sciences

• Article •

March 2016 Vol.59 No.3: 494–505
doi: 10.1007/s11431-015-5968-z

Nonlinear magnetic network models for flux-switching permanent magnet machines

ZHANG Gan, HUA Wei* & CHENG Ming

School of Electrical Engineering, Southeast University, Nanjing 210096, China

Received August 25, 2015; accepted October 26, 2015; published online December 25, 2015

In this paper, firstly, a basic nonlinear magnetic network model considering iron saturations is proposed for a three-phase 12-stator-slot/10-rotor-pole flux-switching permanent magnet (FSPM) machine. This model is built under cylindrical coordinates and enables the open-circuit air-gap flux-density distributions, phase permanent magnet (PM) flux-linkage, and electromotive-force (EMF) to be predicted with acceptable accuracy. However, large discrepancies are found in the predictions of armature inductances. Then, the basic model is modified by taking into account the localized saturation effect. As a result, the electromagnetic performance can be predicted more accurately, especially for the air-gap flux-density distributions. Furthermore, two improved models are proposed by adding bypass-bridge branches in stator network, to enhance the calculating accuracy of both saturated and unsaturated armature inductances. Finally, the predicted results from the four magnetic network models are validated by both 2D finite element analysis (FEA) and experimental measurements on a machine prototype. Overall, comparisons indicate that the model with bypass-bridge branches between stator teeth and back irons exhibits best performances.

air-gap flux density, finite element analysis, flux switching, nonlinear magnetic network, permanent magnet

Citation: Zhang G, Hua W, Cheng M. Nonlinear magnetic network models for flux-switching permanent magnet machines. Sci China Tech Sci, 2016, 59: 494–505, doi: 10.1007/s11431-015-5968-z

1 Introduction

Stator permanent magnet (PM) machines have attracted considerable attention due to their compact and robust rotor structure with both magnets and armature windings located in the stator. Compared to double salient permanent magnet (DSPM) machines [1,2], flux-switching permanent magnet (FSPM) machines exhibit the merits of high torque density, essentially sinusoidal back-EMF waveforms with straight rotor, as shown in Figure 1 [3–7].

Conventionally, finite-element analysis (FEA) is widely used for predicting electromagnetic performances of electrical machines, especially for switched-reluctance machines and PM brushless machines due to the nonlinear saturation in iron, with the developments of commercial software packages, e.g., ANSYS, ANSOFT and FLUX, etc. However, compared with FEA-based analysis method, traditional magnetic circuit-based analysis methods, e.g. nonlinear lumped parameter magnetic circuit (LPMC) [8] and nonlinear magnetic network model (NMNM) [9] are preferred at the primary design stage, due to the acceptable accuracy and considerable computational time saving. In [8], a nonlinear LPMC model was proposed for a 12-stator-slot/10-rotor-pole FSPM machine. Moreover, a hybrid model combining LPMC and the Fourier analysis is introduced in [10,11]. However, the LPMC and hybrid models cannot take into account the localized saturation effect. Although the predicted open-circuit PM flux, average d- and q-axis inductances by LPMC model are validated by FEA with

*Corresponding author (email: huawei1978@seu.edu.cn)

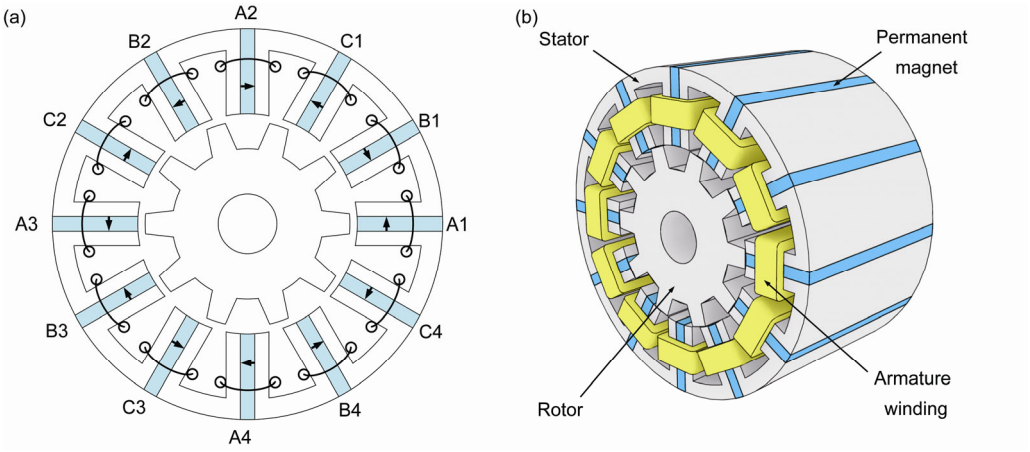

Figure 1 (Color online) Configurations of the 12-stator-pole/10-rotor-pole FSPM machine. (a) Cross section, (b) 3D configuration.

satisfied accuracies, the waveforms of self- and mutual-inductances obtained by LPMC model differ from FEA results by a maximum discrepancy of nearly 18% and 12%, respectively. The inaccurate calculations of inductances would degrade the practicality in analysis of fault-tolerant operation. In addition, the unsaturated inductances, when residual remanence of PMs (B_r) is set to be 0, are not given, which is also critical to fault-tolerant operation when demagnetization occurs to PMs.

Hence, in this paper, a preliminary nonlinear magnetic network model (NMNM, i.e. NM^2) is proposed for a 12-stator-slot/10-rotor-pole FSPM machine with the design details illustrated in Figure 2 and listed in Table 1 [12]. Different from only half FSPM machine being modeled by LPMC based on rectangular coordinates in [8], the whole FSPM machine is modeled by NM^2 based on the polar coordinates in this paper. So the NM^2 exhibits the potential application in fault analysis which may require asymmetrical PM excitations or armature load conditions, e.g., when demagnetization happens to one magnet piece, or short-circuit fault happens to one armature coil. Then, focused on the open- circuit performances, the basic NM^2 is improved in steps by taking into account the localized saturation effect and the leakage flux between stator poles, which can be summarized as follows.

1) The modeling concept and method of the nonlinear magnetic network is introduced in section 2.1, and the resultant model is termed as the Basic-model.

2) In section 2.2, the Basic-model is modified by considering localized saturation effect, which enables the air-gap flux-densities to be calculated more accurately, and the corresponding model is termed as the Modified-model.

3) In section 4, based on the Modified-model, two improved magnetic network models are further proposed by adding bypass-bridge branches to the stator network, to enhance the calculating accuracy of both saturated and unsaturated inductances. These two improved network models are termed as Bypass-bridge-model-1 and -2 (BBM-1 and

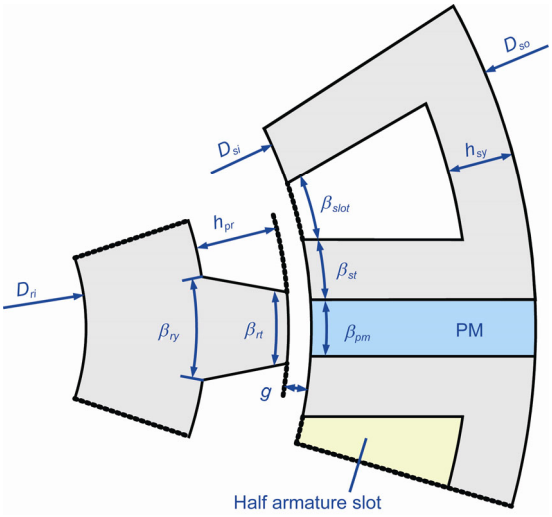

Figure 2 (Color online) Design dimensions of the FSPM machine.

Table 1 Design specification of the FSPM machine

Symbol	Quantity	Parameters
B_r	Magnet residual remanence	1.2 T
H_c	Magnet coercive force	950 kA/m
N_c	Turns per armature coil	75
D_{so}	Stator outer diameter	128 mm
D_{si}	Stator inner diameter	70.4 mm
l_a	Active stack length	75 mm
g	Air-gap length	0.35 mm
D_{ri}	Rotor inner diameter	22 mm
h_{sy}	Stator yoke height	4.6 mm
h_{pr}	Rotor pole height	8.7 mm
P_s	Stator tooth number	12
P_r	Rotor pole number	10
β_{st}	Stator tooth width	7.5°
β_{pm}	PM width	7.5°
β_{rt}	Rotor tooth width	10.5°
β_{ry}	Rotor yoke width	21°

BBM-2), respectively.

4) The performances of the preceding four nonlinear magnetic network models are comprehensively evaluated in section 5, and further validated by experimental measurements on a machine prototype. Overall, the BBM-2 exhibits best performances.

It should be emphasized that, as we know, more details of magnetic network model would result in better accuracy. Thereafter, our purpose is to provide a detailed introduction and procedure on how to build nonlinear network models for FSPM machines, as well as how to balance a trade-off between the acceptable accuracy and the complexity of model structure.

2 Modeling procedure of the magnetic network structures for the FSPM machine

2.1 The basic magnetic network model

The basic equation which governs each element of the magnetic network model is given by

$$\Phi = F \cdot G, \tag{1}$$

where Φ, G, and F are the branch flux, permeance, and magneto-motive-force (MMF), respectively. Meantime,

$$G = \mu_0 \mu_r \frac{S}{l}, \tag{2}$$

where μ_0, μ_r, S, l are the permeability of free space, the relative permeability, cross-section area, and effective stack length, respectively. μ_r is determined by iteration from the B–H curve of the lamination material.

Figure 3 shows the open-circuit field distributions when rotor position is θ_r=0° at d-axis (phase-A PM flux is 0), and θ_r=9° at q-axis (phase-A PM flux is maximum), respectively. The variation of the flux density in the magnets is very small and the permanent magnets can be simply modeled as an equivalent MMF [6], which is given by

$$F_m = \frac{B_r}{\mu_0 \mu_r} h_m, \tag{3}$$

and the permeance of the magnets,

$$G_m = \mu_0 \mu_r \frac{l_m l_a}{h_m}, \tag{4}$$

where h_m and l_m are the magnet thickness and width, respectively, and B_r is the magnet remanence.

Although the permeances of ferromagnetic and PM regions can be calculated by eqs. (1)–(4), determination of the air-gap permeances are much more complicated, which is also the key to predict the air-gap flux density. Figure 4 gives the simplified flux paths in the air-gap region, which are obtained based on the field distributions as shown in Figure 3. The stator and rotor surfaces are assumed to be equipotentials, so the flux paths in Figure 4 are perpendicular to the interfaces between air-gap and irons. Specifically, the flux paths/permeances consist of five types, i.e., those given in Figure 5 along with the corresponding equations [8]. Besides, the calculating methods of permeances between the trapezoidal stator and rotor teeth can be found in [9].

Thus, a complete nonlinear magnetic network model of the FSPM machine (when θ_r=0°), termed as the Basic-model, can be established as shown in Figure 6, which is solved by nodes potential method. More details about the establishing and solving procedures of the magnetic circuit equations were given in [9]. It should be noted that the Basic-model can be modified adaptively according to different rotor positions, due to the changing air-gap permeances.

2.2 The modified magnetic network model

Figure 7 shows the localized saturation effect in the FSPM machine, where the stator tooth is partially overlapped with rotor pole. It can be expected that, the simplified air-gap flux branch in the Basic-model may result in inaccurate predictions of air-gap flux-density distributions. As will be analyzed in section 3, the air-gap flux-densities in these regions without considering localized saturations are far beyond 2 T (Figure 11, Basic-model), which is not realistic. Hence, the Basic-model is modified by taking into account localized saturation effect that appears when a stator tooth is partially overlapped with a rotor pole with the details given in Figure 8. The partially-overlapped stator tooth is divided

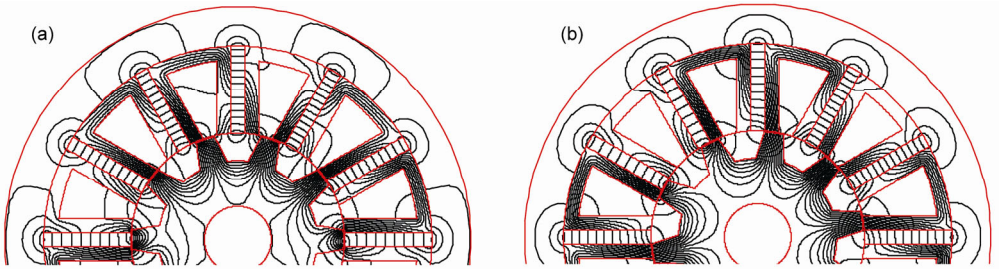

Figure 3 (Color online) Open-circuit field distributions. (a) Rotor position is at d-axis where θ_r=0°; (b) rotor position is at q-axis where θ_r=9°.

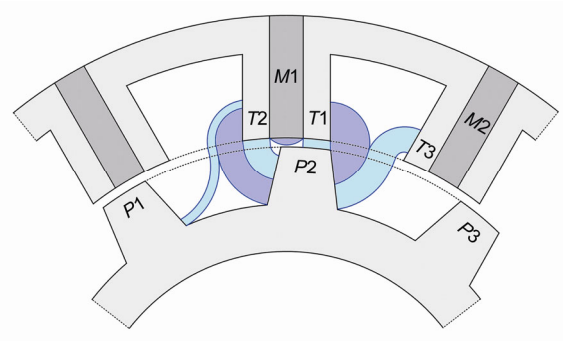

Figure 4 (Color online) Simplified flux paths in air-gap region.

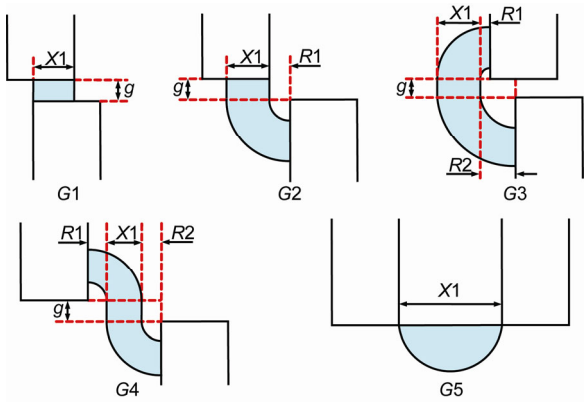

Figure 5 (Color online) Typical air-gap permeances of the FSPM machine, $G_1=(\mu_0 L_a X_1)/g$, $G_2=(2\mu_0 L_a)/(\pi)\ln(1+(\pi X_1)/(\pi R_1+2g))$, $G_3=(\mu_0 L_a/\pi)\ln(1+(2\pi X_1)/(\pi(R_1+R_2)+2g))$, $G_4=(2\mu_0 L_a X_1)/(\pi(R_1+R_2+X_1)+2g))$, $G_5=0.26\mu_0 L_a$.

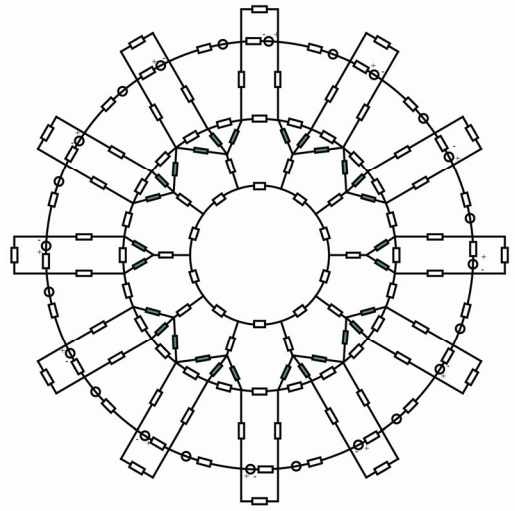

Figure 6 (Color online) The Basic magnetic network model of the FSPM machine when θ_r=0°.

into two portions, and a coefficient named k_{sat} is introduced in to quantitatively express the division portions of the stator tooth:

$$k_{sat}=\frac{h_{sat}}{h_t}, \tag{5}$$

where h_{sat} is the divided region depth, and h_t is the real stator slot depth. Satisfied results can be obtained when 0.3< k_{sat}<0.5. In this paper, k_{sat}=0.4 is adopted in each stator tooth that partially overlapped with one rotor pole. Branches of the related rotor poles are also modified. Besides, a similar solution is introduced in [9], in which the lower half stator pole is divided into two portions.

The modified magnetic network model (when θ_r=0°) is shown in Figure 9 and termed as the Modified-model. Apparently, the network around air-gap in the Modified-model is much more complex than that in the Basic-model. It should be noted that the refined branches in the localized saturated regions have to be adaptively changed according to rotor positions. The electromagnetic performance obtained by the Basic- and Modified-models will be compared with FEA results in the following section.

3 Comparisons of the predicted electromagnetic performances

In this part, the electromagnetic performances obtained by the Basic- and Modified-models are compared with FEA predictions. Comparisons indicate that the open-circuit PM flux can be predicted accurately by both magnetic network models. However, better agreement of the predicted air-gap flux-density distributions is achieved by FEA and Modified-model. Unfortunately, large discrepancies are found between the FEA predicted armature winding inductances and those by magnetic network models.

3.1 Air-gap flux-density distributions

Firstly, Figure 10 shows the FEA calculated open-circuit flux-density distributions at two typical rotor positions where θ_r=0° and θ_r=9°, respectively. Then, the corresponding air-gap flux-density distributions obtained by the Basic- and Modified-models are compared with FEA predictions, as shown in Figure 11. Apparently, the flux-density waveforms in air-gap are far from sinusoidal and exhibit significant harmonics, which are similar to that of switched-reluctance machines (SRMs) due to the doubly-salient structure. In addition, some unreasonable peak values (far beyond 2 T) appear in the air-gap flux-density waveforms where the rotor poles partially overlap the stator poles in Basic-model, when neglecting localized saturations.

However, it can also be seen that the predicted air-gap flux-densities by Modified-model are closer to the FEA results, especially near local peak values (highlighted by dotted circles in Figures 10 and 11). Due to the adaptively varying branches in the corresponding stator teeth and rotor poles according to the rotor positions in Modified-model, the localized saturation effect can be accounted for, which will also be elaborated in section 2.2.

It should be emphasized that the cogging torque can

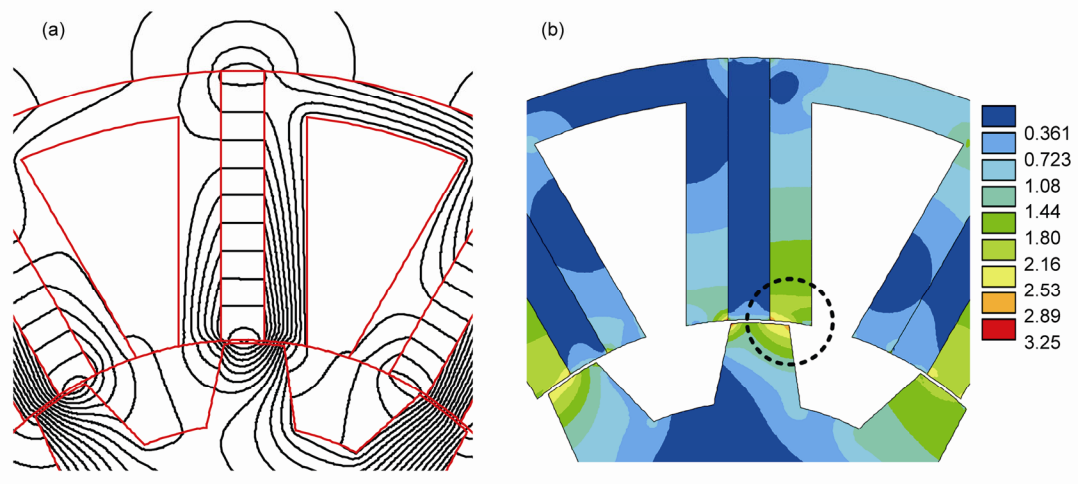

Figure 7 Field distributions and flux-density distributions between stator teeth and rotor poles. (a) Field distributions; (b) flux-density distributions.

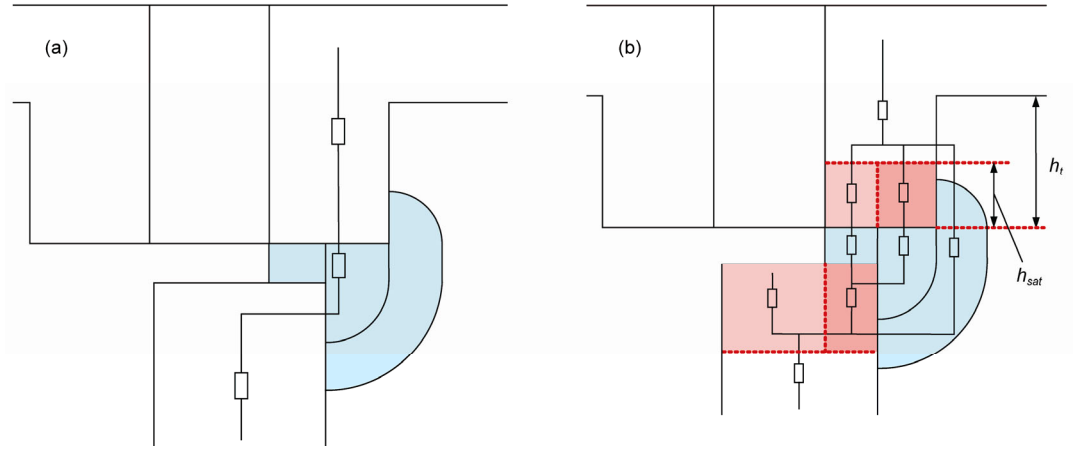

Figure 8 Air-gap permeances between stator tooth and rotor pole in different models. (a) Simplified condition; (b) considering localized saturation effect.

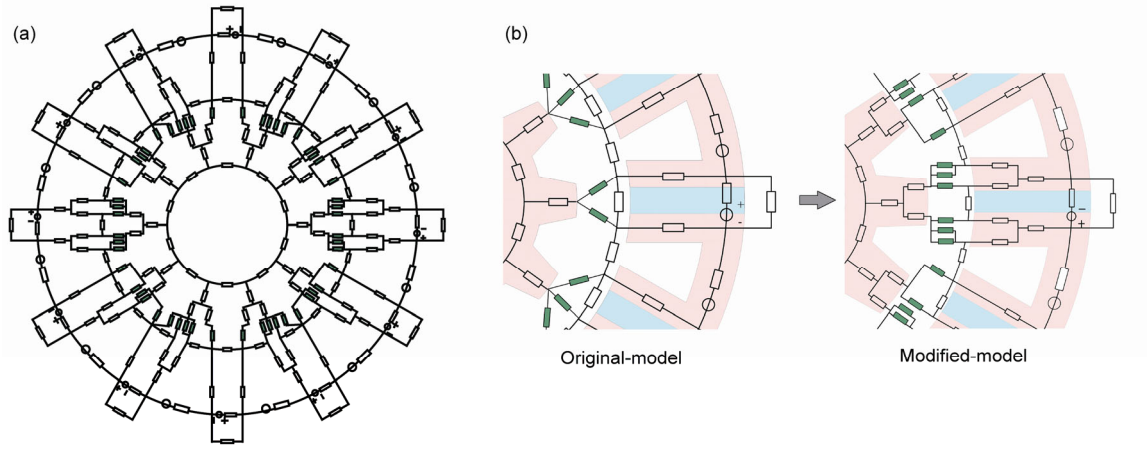

Figure 9 Modified magnetic network model of the FSPM machine. (a) Modified magnetic network model when θ=0°; (b) detailed comparison.

hardly be calculated by integrating the Maxwell stress tensor over rotor surface [11,13,14] based on the NM^2. Since the required radial and tangential components of air-gap flux- density distributions cannot be directly obtained due to the simplified air-gap flux tubes, which assume that the air-gap flux vectors are in radial direction and perpendicularly

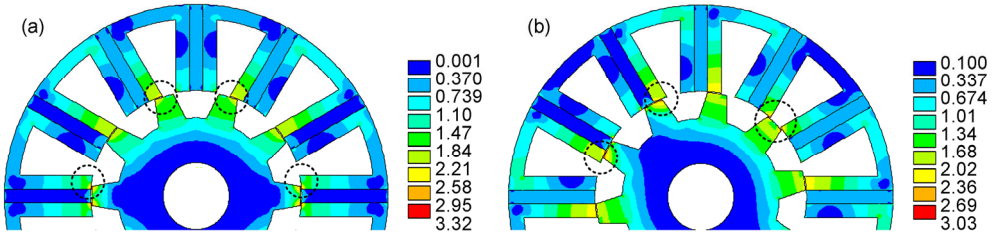

Figure 10 Flux-density distributions of half FSPM machine. (a) Rotor position at d-axis where θ_r=0°; (b) rotor position at q-axis where θ_r=9°.

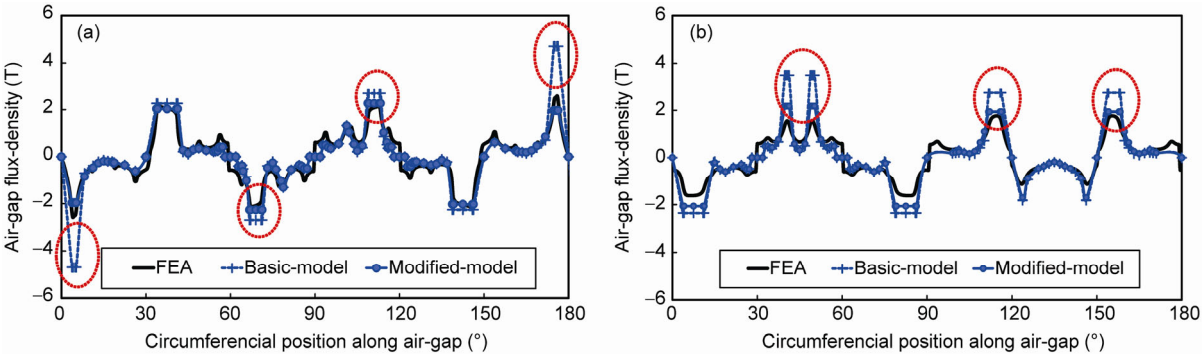

Figure 11 Comparisons of the open-circuit air-gap flux-density distributions of half FSPM machine. (a) Rotor position θ_r=0°; (b) rotor position θ_r=9°.

passing through the rotor surface.

3.2 Open-circuit phase PM flux and EMF waveforms

The armature coil PM flux-linkage ψ_{PM} can be predicted directly from the magnetic network models and the resultant back-EMF is determined from

$$e = -\frac{\mathrm{d}\psi_{PM}}{\mathrm{d}t}. \tag{6}$$

The open-circuit coil flux and back-EMF waveforms in one electrical period calculated by the magnetic models and FEA are compared in Figure 12 with good agreements. However, better performance is exhibited by the Modified-model, especially for the coil back-EMFs, due to increased elements number and consequently more accurate air-gap flux-density distributions.

3.3 Armature winding inductances

The phase self- and mutual-inductances can be obtained from phase flux-linkage variation with armature current, i.e.,

$$L_{aa} = \frac{\psi_{a\_I_a} - \psi_{a\_0}}{I_a}, \tag{7}$$

$$M_{ab} = \frac{\psi_{b\_I_a} - \psi_{b\_0}}{I_a}, \tag{8}$$

where L_{aa} is the self-inductance of phase-A, M_{ab} is the mutual-inductance between phase-A and phase-B, ψ_{a_0} and ψ_{b_0} are the phase PM flux-linkages of phase-A and phase-B, respectively due to magnets only, ψ_{a_Ia} and ψ_{b_Ia} are the combined flux-linkages of phase-A and phase-B, respectively, due to magnets and phase-A current I_a.

Figure 13 shows the coil fluxes when phase-A is loaded by a current density of J_{sa}=10 A/mm^2, with a slot package factor of k_{pf}=0.6 and half slot area of S_a=133.3 mm^2, i.e., corresponding to 800 AT per half slot (800 AT=J_{sa}×k_{pf}×S_a=10 A/mm^2×0.6×133.3 mm^2, where AT is ampere turn). As can be seen, the NM^2-based fluxes differ greatly from that of FEA, especially for the Basic-model. Consequently, large discrepancies are found in the predicted armature winding inductances as shown in Figure 14. In the case of unsaturated inductances (by setting PM remanence B_r=0), a relatively considerable error exists in the predicted L_{aa} vs. rotor positions waveforms from both magnetic models and FEA, which can be attributed to the simplification of leakage flux paths between stator poles, as will be further discussed in section 4.

It should be emphasized that the applied 800 AT per half slot is relatively high, due to the following two considerations.

1) The armature reactions on permanent magnetic field are more obvious when a high armature current is applied, thus easier to be observed by FEA.

2) Relatively high current may be applied when water-cooling is employed or under over-load operation conditions.

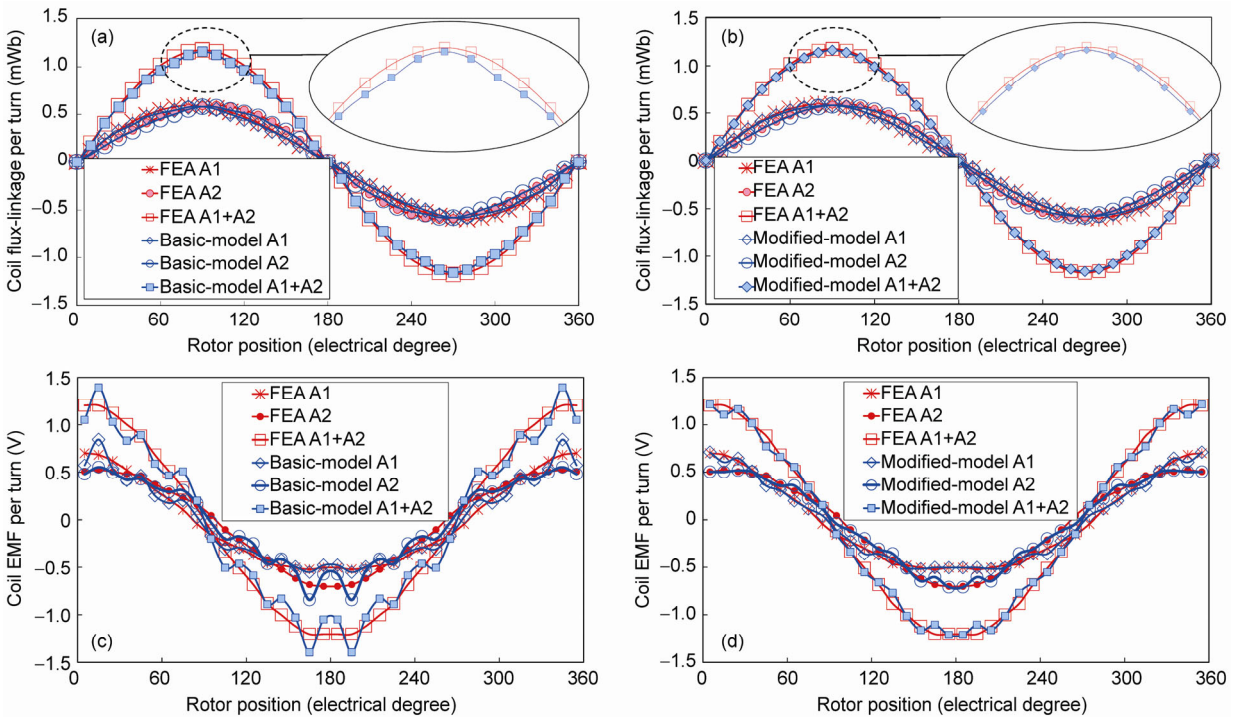

Figure 12 (Color online) Comparisons of the open-circuit PM fluxes and EMFs at 1000 r/min. (a) Fluxes predicted by FEA and Basic-model; (b) fluxes predicted by FEA and Modified-model; (c) EMFs predicted by FEA and Basic-model; (d) EMFs predicted by FEA and Modified-model.

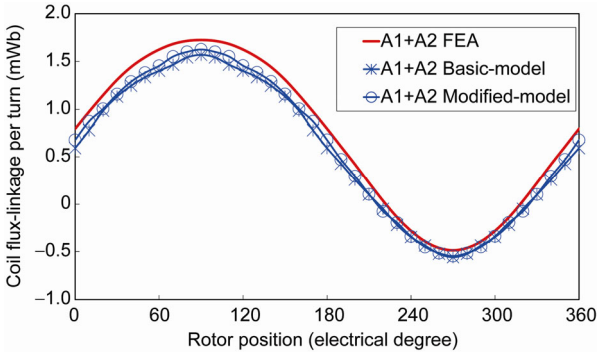

Figure 13 (Color online) Comparison of coil fluxes when only phase-A is loaded by 800 AT per half slot.

4 Improved magnetic network models

In this section, two improved network models are proposed based on the Modified-model, which enables the inductances to be calculated more accurately.

4.1 Improving method based on the modified-model

Figure 15 shows the FEA-based field distributions when only phase-A is loaded by 800 AT per half slot. Compared to the open-circuit condition, more flux leakages can be found in armature slots. However, these flux leakages are not effectively considered by both Basic- and Modified-models.

Hence, two improved models are proposed based on the Modified-model, by adding bypass-bridge branches to the stator network, to provide flux paths for armature flux leakage and thus enhance the predicting accuracy of inductances. These improved models are termed Bypass-bridge-model-1 and -2 (BBM-1 and BBM-2), as shown in Figure 16. Pacifically, in BBM-1, each PM branch is divided into three parallel ones, and two bypass-bridges are added across each slot, as shown in Figure 16(b). While in BBM-2, each stator back iron branch is divided into series ones, and two bypass-bridges are added between the stator teeth and back irons, as shown in Figure 16(d). Unlike the parallel bypass-bridges in the BBM-1, the added bypass-bridges across one slot are in series in BBM-2. Each armature MMF source is also divided into series ones. Determining methods of the bypass-bridge permeances refer to those in Figure 5. It should be emphasized that the permeances of the bypass-bridge are quite small compared to back iron ones. So, as will be analyzed in the followings, satisfied accuracy can be obtained by placing the current-related MMF sources on back-iron branches.

Observing Figure 15, it should be noticed that, the phase-A current will generate two types of flux leakages, namely those between stator teeth as given by Figure 15(a), and those between stator back irons and stator teeth as given by Figure 15(b). The bypass-bridges of BBM-2 enable both types of flux-leakages being considered. However, the BBM-1 can only take into account the flux leakages shown in Figure 15(a). Besides, since phase-A current is applied on

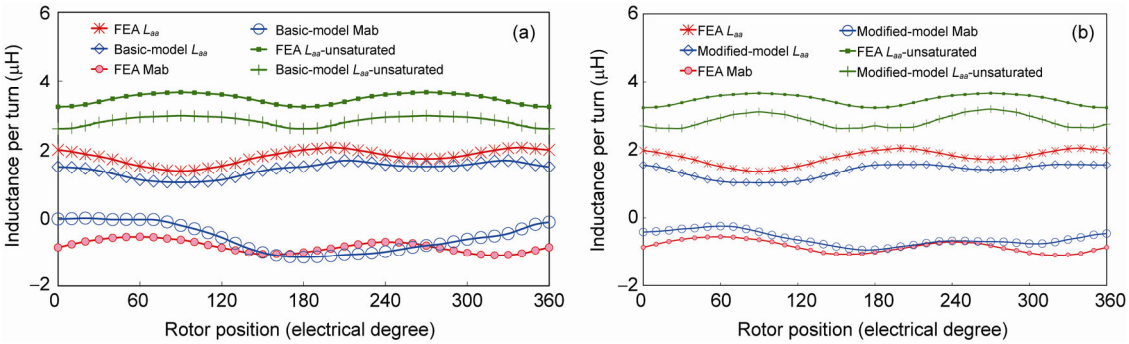

Figure 14 (Color online) Comparisons of the armature inductances. (a) Predicted by FEA and Basic-model; (b) predicted by FEA and Modified-model.

half slot, it is more accurate to place the corresponding MMF sources on one of the two series iron back branches, as in BBM-2. The previous analysis indicates that the BBM-2 might be more accurate when armature currents are applied, e.g., when calculating the inductances, which would be validated by FEA results in the following section.

4.2 Predictions by BBM-1 and BBM-2

In this part, the predictions of the two improved models are compared with FEA results. Then, a comprehensive evaluation of the established four magnetic network models is presented.

4.2.1 Open-circuit performances

Figures 17 and 18 compare the predicted open-circuit air-gap flux-density distributions and coil fluxes and EMFs with satisfied agreement. But a slightly larger harmonic content can be found in the BBM-1 predicted coil EMF waveforms, as shown in Figure 18(c), although the combined coil-A1+coil-A2 EMFs are much more accurate. Meanwhile, compared to the Modified-model, the BBM-2 predicted coil EMF waveforms are more close to the FEA results near peak values. This reveals that the BBM-2 can effectively take into account PM flux leakages between stator teeth and back irons, due to the added bypass-bridges.

4.2.2 Armature winding inductances

Figure 19 shows the coil flux when only phase-A is loaded by 800 AT per half slot, and Figure 20 compares the inductances. Observing Figure 20(a), the BBM-1 calculated saturated self- and mutual-inductances are much more accurate than those by the Modified-model. Although more complex than the Modified-model, the BBM-1 is still unable to take into account the flux-leakages between the stator back irons and stator teeth, which is more significant under unsaturated condition. This will result in the inaccurate calculated unsaturated inductances. In addition, the MMF source due to phase-A current is applied on the whole back iron branch, which will further contribute to the inaccuracies. At the same time, both saturated and unsaturated inductances obtained by BBM-2 highly agree with FEA results, meantime are more accurate than those by BBM-1, as shown in Figure 20(b). This verifies the effectiveness of bypass-bridges branches in the BBM-2 as analyzed in Section 4.1. Overall, considering the satisfied performances in open-circuit calculations, the BBM-2 exhibits the best potential to be built into a general design and analysis application/software of FSPM machine.

4.2.3 Comprehensive evaluations of four models

A comprehensive comparison of the discrepancies between predictions by each magnetic network model and by FEA is listed in Table 2. As can be seen, the BBM-2 exhibits best overall performances, thus greatest potential in application. Additionally, the calculating time in one electrical period (total 72 steps) of different methods are listed in Table 3. The extremely short time consuming of NM^2 can be explained as:

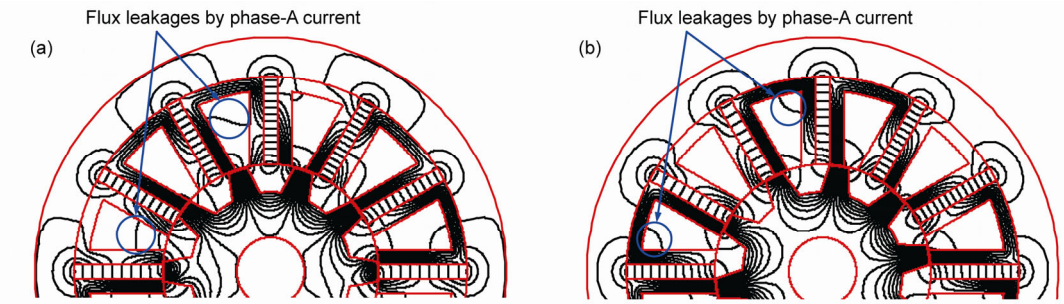

Figure 15 (Color online) Field distributions when phase-A is loaded by 800 AT per half slot. (a) Rotor position at *d*-axis where θ_r=0°; (b) rotor position at *q*-axis where θ_r=9°.

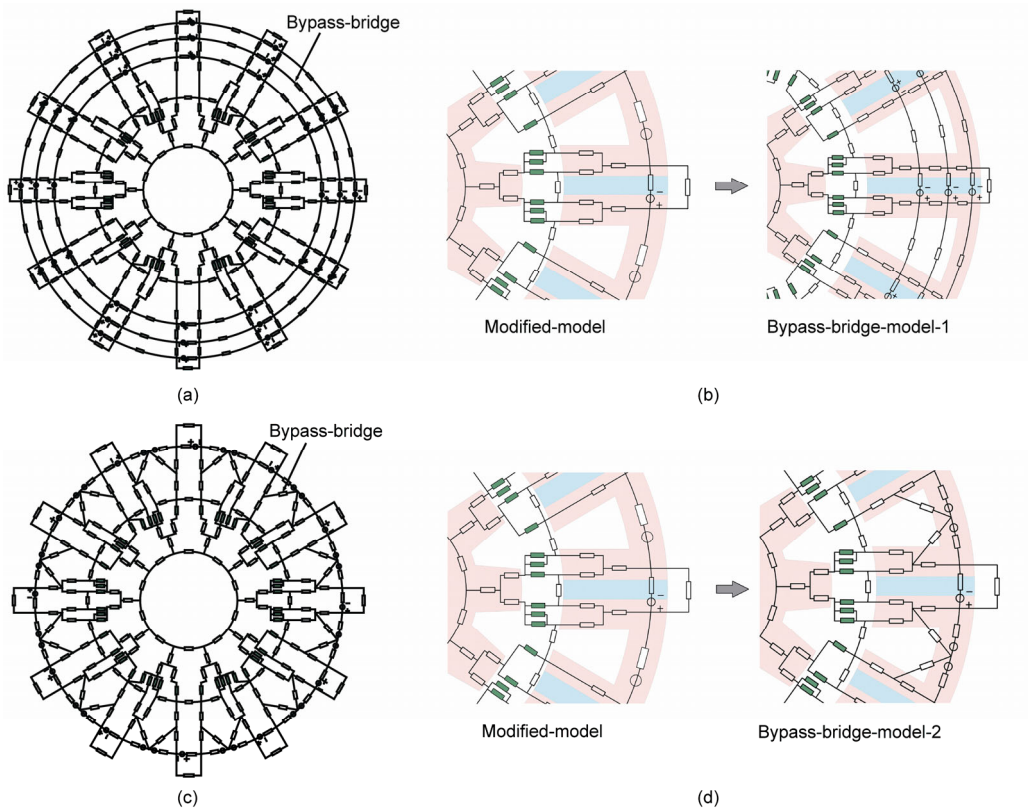

Figure 16 (Color online) The Bypass-bridge-model-1 (BBM-1) and Bypass-bridge-model-2 (BBM-2) of the FSPM machine. (a) Bypass-bridge-model-1 when θ_r=0°; (b) detailed comparison of BBM-1; (c) bypass-bridge-model-2 when θ_r=0°; (d) detailed comparison of BBM-2.

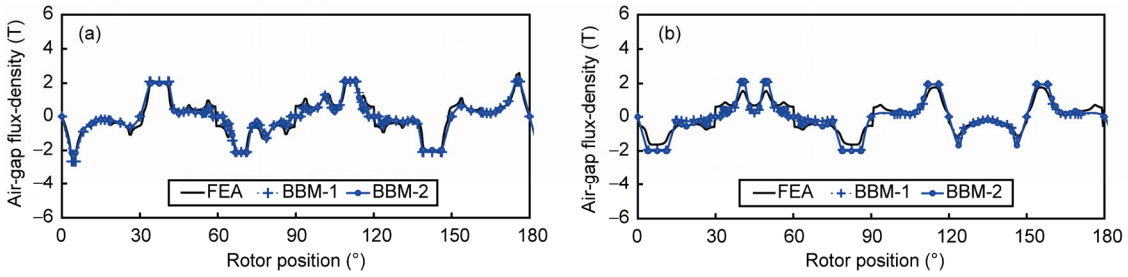

Figure 17 (Color online) Comparisons of open-circuit air-gap flux-density distributions of half FSPM machine. (a) Rotor position θ_r=0°; (b) rotor position θ_r=9°.

At each rotor position, the degree-of-freedoms (DOF) of the final equations in the nonlinear network and FEA model can be assumed to be approximately equal nodes number, respectively. On the other hand, greater DOF means greater time consuming to solve the equations. As can be found in Table 3, the number of DOF in the magnetic network models is significantly less than that in the FEA model (in commercial software ANSYS), resulting in a much shorter calculating time required by the magnetic network models. Additionally, the calculations are carried out on a PC computer with a Core i3 CUP (2.0 GHz) and 4 G RAM.

5 Experimental validations

A prototype of the 12-stator-slot/10-rotor-pole FSPM machine is manufactured as shown in Figure 21. The open-circuit phase-A EMF waveforms (75 turns per armature coil at 1000 r/min) obtained from the magnetic network models and FEA are compared with experimental measurements in Figure 22 with good agreements, verifying the effectiveness of FEA method and the proposed magnetic network models. The calculated and measured phase-A self-inductances are compared in Figure 23 and the total discrepancies between results by each method and experimental measurements are listed in Table 4. As can be seen, the closest results to measurements are obtained by FEA and BBM-2, which consist with the above analysis. It should be emphasized that due to the restrictions of the LCR meter, the inductances are measured when a low current of 80 mA is applied, corresponding to 8 AT per half slot. Additionally, it can be noticed that the measured phase-A EMF is slightly lower

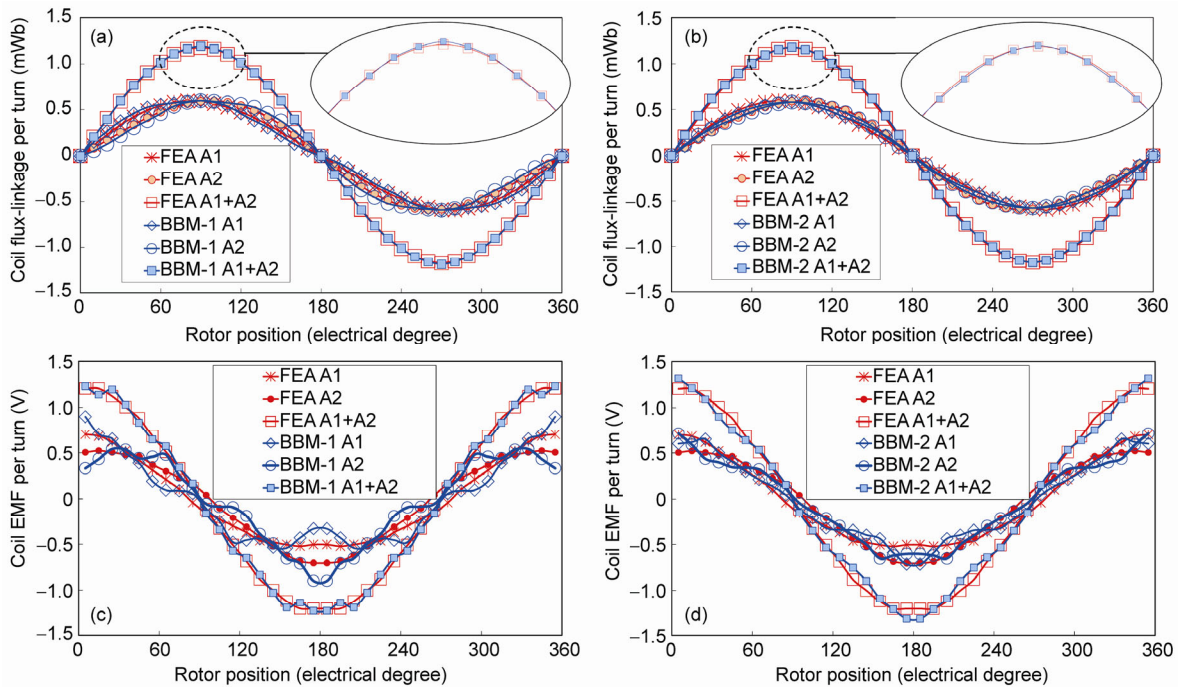

Figure 18 (Color online) Comparisons of the open-circuit PM fluxes and EMFs at 1000 r/min. (a) Fluxes predicted by FEA and BBM-1; (b) fluxes predicted by FEA and BBM-2; (c) EMFs predicted by FEA and BBM-1; (d) EMFs predicted by FEA and BBM-2.

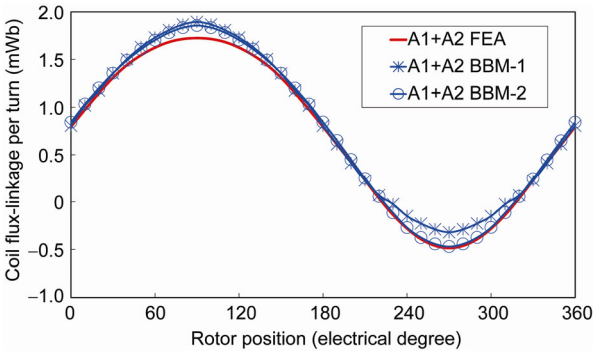

Figure 19 (Color online) Comparison of the coil flux when phase-A is loaded by 800 AT per half slot.

than 2D FEA predictions, partially due to the 3D end-effect [10,15–17]. Also, satisfied agreement is found between the measured and 2D FEA calculated inductances considering manufacturing tolerances. In addition, the FEA predicted (considering 3D end-effect) and measured peak-to-peak values of cogging torque are 2.8 and 2.4 Nm, respectively.

6 Conclusion

In this paper, a nonlinear magnetic network model is proposed for a three-phase 12-stator-slot/10-rotor-pole FSPM machine, and named the Basic-model. This network model is built in cylindrical coordinates considering iron saturations, and enables the electromagnetic performances, e.g., armature coil flux and air-gap flux-density distribution to be calculated. Then, the Basic-model is improved by taking into account localized saturation effect, thus resulting in the

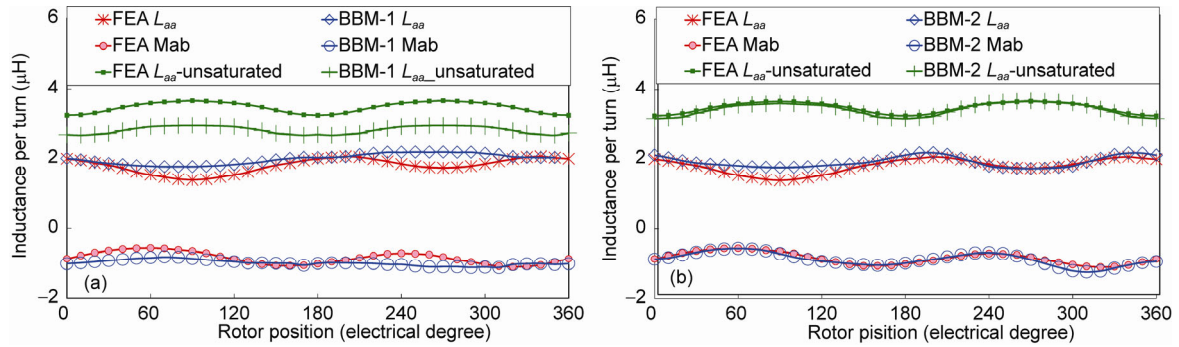

Figure 20 (Color online) Comparisons of the armature inductances. (a) Predicted by FEA and BBM-1; (b) predicted by FEA and BBM-2.

Table 2 Discrepancies of results by magnetic network models and FEA

Air-gap flux-density where θ_r=0° (%)	Basic-model: 33	BBM-1: 12
	Modified-model: 13	BBM-2: 12
Air-gap flux-density where θ_r=9° (%)	Basic-model: 47	BBM-1: 24
	Modified-model: 27	BBM-2: 23
Peak phase-A flux (%)	Basic-model: −1.3	BBM-1: +1.3
	Modified-model: −1.3	BBM-2: +0.4
THD of phase-A flux (%)	Basic-model: +7.4	BBM-1: −1.9
	Modified-model: +1.9	BBM-2: +1.9
Saturated average L_{aa} per turn (%)	Basic-model: −33.0	BBM-1: +10.5
	Modified-model: −25.2	BBM-2: +0.4
Saturated average M_{ab} per turn (%)	Basic-model: −40.1	BBM-1: +15.3
	Modified-model: −27.2	BBM-2: +3.5
Unsaturated average L_{aa} per turn (%)	Basic-model: −12.7	BBM-1: −14.1
	Modified-model: −13.1	BBM-2: −0.1

Table 3 Computing time of one electrical period and the degree-of-freedom (DOF) of equations in each step

Time consuming	Basic-model: 3.2 s	BBM-1: 4.8 s
FEA: 52 min	Modified-model: 4.1 s	BBM-2: 4.7 s
DOF of equations	Basic-model: 101	BBM-1: 170
FEA: 268524	Modified-model: 146	BBM-2: 158

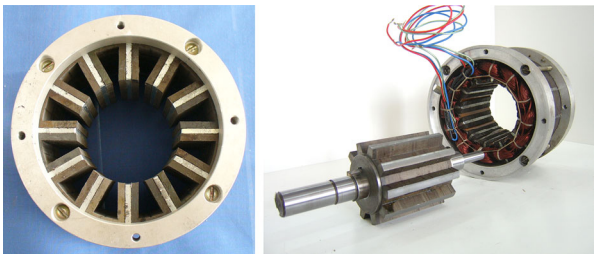

Figure 21 (Color online) The 12-stator-slot/10-rotor-pole FSPM machine prototype.

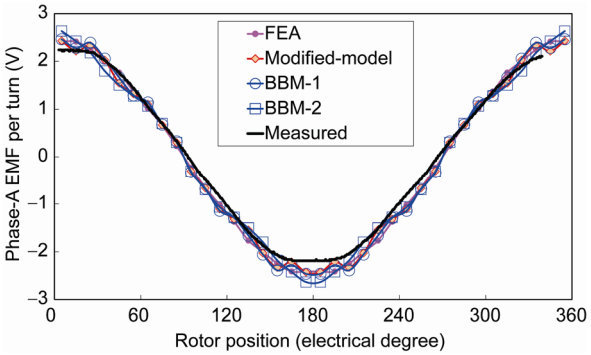

Figure 22 (Color online) Open-circuit phase-A EMF waveforms per turn at 1000 r/min.

Modified-model which gives more accurate predictions of air-gap flux-densities. However, the armature inductances predicted by both the Basic- and Modified-models differ greatly from FEA results. Thus, to enhance the calculating

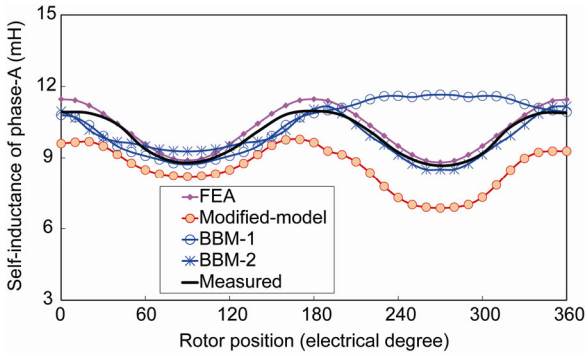

Figure 23 (Color online) Comparison of calculated and measured phase-A self-inductances (75 turns per armature coil).

Table 4 Discrepancies of predicted inductances with measurements

FEA	Modified-model	BBM-1	BBM-2
3.1%	20.7%	11.6%	3.4%

accuracy of both saturated and unsaturated inductances, two improved models considering flux leakages between stator teeth and back irons are further proposed and validated by FEA.

A comprehensive comparison of the preceding four magnetic network models reveals that, best overall performances and potentials are exhibited by the model with by-pass-bridge branches between stator teeth and back irons, i.e. the BBM-2. Finally, the predictions by the magnetic network models and FEA are validated by experimental meas-

urements on a FSPM machine prototype with satisfied agreements.

This work was supported by the National Basic Research Program of China ("973" Project) (Grant No. 2013CB035603), the National Natural Science Foundation of China (Grant Nos. 51177013 & 51322705), Qing Lan Project of Jiangsu Province, Six Talents Climax Project of Jiangsu Province (Grant No. 2011-ZBZZ-036), Technology R&D Program of Jiangsu Province (Grant Nos. BE2012100 & BY2012195), and "333 Talents Project" of Jiangsu Province.

1 Zhu X Y, Cheng M. Design, analysis and control of hybrid excited doubly salient stator-permanent-magnet motor. Sci China Tech Sci, 2010, 53: 188–199
2 Cheng M, Zhou E. Analysis and control of novel split-winding doubly salient permanent magnet motor for adjustable speed drive. Sci China Tech Sci, 2001, 44: 353–364
3 Rauch S E, Johnson L J. Design principles of flux-switching alternators. AIEE T, 1955, 74: 1261–1268
4 Hoang E, Ben-Ahmed A H, Lucidarme J. Switching flux permanent magnet polyphased synchronous machines. In: Proc. 7th Europe Conf. Power Electron and Appl, Aalborg: IEEE Power Electronics Society, 1997
5 Cheng M, Zhang G, Hua W. Overview of stator permanent magnet brushless machine systems and their key technologies (in Chinese). P CSEE, 2014, 34: 5204–5220
6 Yan J H, Lin H Y, Zhu Z Q, et al. Cogging torque optimization of flux-switching transverse flux permanent magnet machine. IEEE T Magn, 2013, 49: 2169–2172
7 Cheng M, Hua W, Zhang J Z, et al. Overview of stator-permanent magnet brushless machines. IEEE T Ind Electron, 2011, 58: 5078–5101
8 Zhu Z Q, Pang Y, Howe Y, et al. Analysis of electromagnetic performance of flux-switching permanent magnet machines by non-linear adaptive lumped parameter magnetic circuit model. IEEE T Magn, 2005, 41: 4277–4287
9 Cheng M, Chau K T, Chan C C, et al. Nonlinear varying-network magnetic circuit analysis for doubly salient permanent-magnet motors. IEEE T Magn, 2000, 36: 339–348
10 Ilhan E, Gysen B L J, Paulides J J H, et al. Analytical hybrid model for flux switching permanent magnet machines. IEEE T Magn, 2010, 46: 1762–1765
11 Gysen B L J, Ilhan E, Meessen K J, et al. Modeling of flux switching permanent magnet machines with Fourier analysis. IEEE T Magn, 2010, 46: 1499–1502
12 Hua W, Cheng M, Zhu Z Q, et al. Analysis and optimization of back-EMF waveform of a flux-switching permanent magnet motor. IEEE T Energy Conv, 2008, 23: 727–733
13 Lubin T, Mezani S, Rezzoug A. 2-D exact analytical model for surface-mounted permanent-magnet motors with semi-closed slots. IEEE T Magn, 2011, 47: 479–492
14 Fei W Z, Luk P C K, Shen J X. Torque analysis of permanent-magnet flux switching machines with rotor step skewing. IEEE T Magn, 2012, 48: 2664–2673
15 Chen J T. Zhu Z Q, Howe D. Stator and rotor pole combinations for multi-tooth flux-switching permanent-magnet brushless ac machines. IEEE T Magn, 2008, 44: 4659–4667
16 Hua W, Cheng M, Zhu Z Q. Comparison of electromagnetic performance of brushless motors having magnets in stator and rotor. J Appl Phys, 2008, 103: 07F124
17 Chau K T, Chan C C, Liu C. Overview of permanent-magnet brushless drives for electric and hybrid electric vehicles. IEEE T Ind Electron, 2008, 55: 2246–2257